

(Phys. Rev. B *in press*)**Hydrostatic pressure response of an oxide two-dimensional electron system**J. Zabaleta,¹ V.S. Borisov,² R. Wanke,¹ H.O. Jeschke,² S.C. Parks,¹ B. Baum,¹ A. Teker,¹ T. Harada,¹ K. Syassen,¹ T. Kopp,³ N. Pavlenko,^{1,3} R. Valentí,² and J. Mannhart¹¹*Max Planck Institute for Solid State Research, 70569 Stuttgart, Germany*²*Institute of Theoretical Physics, Goethe University, 60438 Frankfurt am Main, Germany*³*Center for Electronic Correlations and Magnetism, University of Augsburg, 86135 Augsburg, Germany*

(Dated: May 30, 2016)

Two-dimensional electron systems with fascinating properties exist in multilayers of standard semiconductors, on helium surfaces, and in oxides. Compared to the two-dimensional (2D) electron gases of semiconductors, the 2D electron systems in oxides are typically more strongly correlated and more sensitive to the microscopic structure of the hosting lattice. This sensitivity suggests that the oxide 2D systems are highly tunable by hydrostatic pressure. Here we explore the effects of hydrostatic pressure on the well-characterized 2D electron system formed at LaAlO₃-SrTiO₃ interfaces¹ and measure a pronounced, unexpected response. Pressure of ~ 2 GPa reversibly doubles the 2D carrier density n_s at 4 K. Along with the increase of n_s , the conductivity and mobility are reduced under pressure. First-principles pressure simulations reveal the same behavior of the carrier density and suggest a possible mechanism of the mobility reduction, based on the dielectric properties of both materials and their variation under external pressure.

PACS numbers: 73.40.-c, 62.50.-p, 73.20.-r, 77.22.Ch

I. INTRODUCTION

Pressure is a powerful tool to study and tailor the properties of solids (for reviews, see e.g. Refs. 2,3). In state-of-the-art field effect transistors, for example, epitaxial strain is applied to enhance the electron mobility in silicon and thereby to raise the switching speed. In quantum cascade lasers, layer-straining is used to tailor the band structure for optimal performance.² Hydrostatic pressure has furthermore been applied to induce superconductivity in H-S compounds with reported transition temperatures as high as 203 K.⁴ Striking changes of the electronic properties upon application of pressure have also been found in oxides, which due to their structural degrees of freedom are intrinsically even more sensitive to lattice strain than conventional semiconductors. To give but a few examples, crystal fields, orbital occupancy, polarizations, and exchange coupling in oxides are influenced substantially by slight distortions of ionic sublattices. Pressure-induced changes of the structural and electronic properties have been investigated extensively in bulk oxides and have been demonstrated for thin films. By applying an epitaxial biaxial strain of $\sim 0.9\%$, for example, nominally paraelectric SrTiO₃ films have been turned into ferroelectrics with a T_c of 293 K.⁵ The study of the effects of epitaxial strain in LaAlO₃-SrTiO₃ heterostructures revealed that the critical thickness of the LaAlO₃ layer required to generate the 2D electron systems (2DES) and their carrier concentration depend on the epitaxial strain of the SrTiO₃.⁶⁻⁸ To open a new route for the exploration of the electronic properties of complex oxides under tunable uniaxial and biaxial stress, a novel piezo-based technique is currently being developed.⁹

Uniaxial and biaxial stress change the shapes of the unit cells but alter their volumes only little. For this reason, they do not provide an option to explore and benefit from those electronic effects that are induced by volume changes of the unit cell. These changes are accessible and have been explored by applying hydrostatic pressure. For example, in cuprate high- T_c superconductors the record T_c of 164 K was induced by a pressure of 15 GPa,^{3,10} which enhanced the charge transfer between the CuO₂ layers and off-layer structural units. More recently, the Curie temperature of SrRuO₃ films was reduced from 150 to 77 K by applying hydrostatic pressure up to 23 GPa.¹¹ In bulk n-doped SrTiO₃ a non-monotonic dependence of carrier density and mobility was measured in pressure ranges ≤ 1 GPa.¹² Whereas the above-mentioned studies of the effects of hydrostatic pressure on oxides focused on the properties of three-dimensional electron systems, we study here the pressure effects on a 2DES.

The 2DES at the interface between LaAlO₃ and SrTiO₃, two band insulators, has been widely investigated since its discovery in 2004.¹ It has served as a model system to study the origin of conducting layers at oxide interfaces and has shown a rich phenomenology, including the coexistence of magnetism and superconductivity (for an overview, see, e.g. Ref. 13). A polar discontinuity develops at the interface between TiO₂-terminated, (001)-oriented SrTiO₃ and LaAlO₃. For LaAlO₃ layers with a thickness exceeding 3 unit cells (u.c.),¹⁴ the resulting electric field moves charge carriers from the surface of the LaAlO₃ to the interface, where an n-type 2DES is formed for the TiO₂ termination of SrTiO₃. The formation of the 2DES and its properties can be influenced

by the presence of defects such as oxygen vacancies (for an overview, see e.g. Refs. 15–17). At ambient pressure the electrons at the interface occupy the t_{2g} Ti 3d levels, split by 50 meV into low-energy d_{xy} and higher-energy d_{xz} and d_{yz} bands.^{18,19}

Pressure acting on perovskite-related oxides compresses bonds and modifies the internal structural parameters. For the LaAlO_3 - SrTiO_3 bilayers, the hydrostatic pressure superimposes the stress resulting from the lattice mismatch of $\sim 3\%$ and decreases it. The influence of epitaxial strain on the 2DES was addressed in first-principles model calculations of surface-free heterostructures by Nazir *et al.*^{7,8} and experimentally by Bark and collaborators.⁶ The latter group found that while the carrier concentration is reduced in compressively-strained SrTiO_3 as a result of dipole formation within the SrTiO_3 , no 2DES is formed on tensile-strained SrTiO_3 . These results immediately lead to the question of how the interface 2DES is modified by hydrostatic pressure. Owing to the unit-cell compression it may significantly differ from the response to epitaxial strain.

In this work we combine experimental observations with first-principles electronic structure calculations to study the effect of pressure on the microstructure of the LaAlO_3 - SrTiO_3 interface and its implications on the electronic properties of the 2DES (see Fig. 1). We find that the lattice reconstruction in the LaAlO_3 film, which acts against the interface charge, is partially suppressed by the external pressure thereby reducing the lattice screening of the polar discontinuity and enhancing charge transfer towards the oxide interface. This mechanism sheds light on the reversible increase of the carrier concentration of the 2DES measured in transport experiments up to ~ 2 GPa. This observation has been also confirmed in recent independent experimental work by D. Fuchs *et al.*²⁰ Furthermore, our calculations of static dielectric properties in LaAlO_3 and SrTiO_3 under pressure indicate a reduction of carrier mobility as observed in our measurements. The behavior of this oxide system is opposite in sign to the pressure response of semiconductor

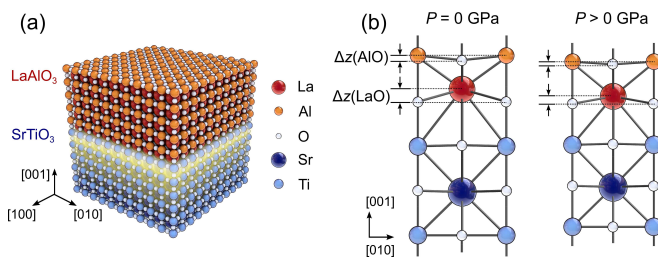


FIG. 1: Illustration of the atomic structure of the LaAlO_3 - SrTiO_3 interface. Panel (a) shows a sketch of the heterostructure with the 2DES at the interface marked in yellow. Panel (b) illustrates the displacements $\Delta z(\text{LaO})$ of the La^{3+} and O^{2-} ions in the LaO sublayer and of the Al^{3+} and O^{2-} ions in the AlO_2 sublayer, $\Delta z(\text{AlO})$. Hydrostatic pressure reduces $\Delta z(\text{LaO})$ and $\Delta z(\text{AlO})$. The much smaller ionic displacements in the SrTiO_3 are not indicated.

quantum wells,²¹ where the carrier concentration is found to decrease with increasing pressure (see Fig. 13 in the Supplement). Our findings reveal that, in contrast to biaxial strain, hydrostatic pressure is a suitable tool for enhancing the carrier density of the 2DES in this oxide system.

II. METHODS

A. Sample growth, pressure cells and transport measurements

Samples were grown by pulsed laser deposition from single-crystal LaAlO_3 targets onto TiO_2 -terminated SrTiO_3 single-crystal substrates at 800°C and 8×10^{-5} mbar O_2 partial pressure followed by two annealing steps at 600°C and 400°C for 1 h at 400 mbar of O_2 partial pressure. The thickness of the LaAlO_3 layer was monitored by in-situ reflective high-energy electron diffraction. Samples were patterned into van der Pauw configurations and into $100\text{ }\mu\text{m}$ -wide Hall bridges by optical lithography and Ar ion sputtering, with electron-beam evaporation used to deposit Ti-Au contacts into the buried electron system (Fig. 2(a),(b)). Patterning and contacting was done as described in Ref. 22, except for using 50 nm of polycrystalline and 6 unit cells of epitaxial LaAlO_3 . Hydrostatic pressure was applied using either a diamond anvil cell or a piston cylinder cell. In the diamond anvil cell transport measurements the heterostructure samples are encased between the small tips of the diamonds. Therefore, several series of LaAlO_3 - SrTiO_3 samples were fabricated and cut to typical sizes of $350 \times 350 \times 65\text{ }\mu\text{m}^3$ (Fig. 2(a),(c)). As the piston cylinder cell allows larger samples, the typical size of the samples used for the piston cell measurements was the $1 \times 1 \times 0.2\text{ mm}^3$ (Fig. 2(a),(b)). Control measurements confirmed that the sample properties were not affected by the cutting (see Supplement Fig. 14).

As illustrated in Fig. 2(d), we used diamonds of 1.25 and 1.5 mm tip diameters. Inconel gaskets (250 μm thick) were pre-pressed, drilled, and then insulated with a mixture of Stycast 1266 and Al_2O_3 powder. The gasket hole had a diameter of between 850-900 μm and an initial height of 170-200 μm . The cleaned diamond surface of the lower anvil was patterned with a metallic trilayer (50 nm Ti/50 nm Pt/500 nm Au) by electron-beam evaporation through a stainless-steel shadow mask. Contacts were annealed in vacuum at 650°C for 20 min. Daphne 7373 oil was used as pressure medium; the pressure was measured using ruby luminescence. Measurements with a piston cylinder cell (Almax Easy Labs) were also performed using a manganin coil as pressure sensor and Daphne 7373 as pressure medium.

To avoid photo-excited carriers, all transport measurements were performed in darkness, after keeping the samples dark for at least 12 h. Prior to the application of pressure, all samples were characterized by transport

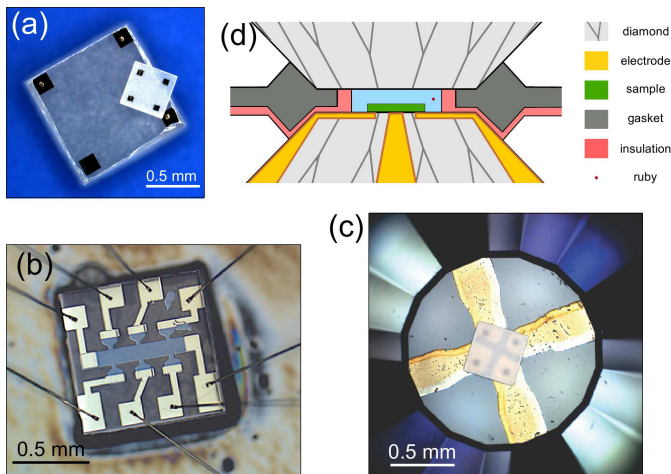


FIG. 2: (a) Optical microscopy image showing samples for both a diamond anvil cell (small sample) and for the piston cylinder cell (large sample). Both samples are in a van-der-Pauw configuration. (b) Optical micrograph of a sample with a patterned and contacted Hall bar. The sample is $1 \times 1 \times 0.2 \text{ mm}^3$ in size and the Hall bar is $100 \mu\text{m}$ wide. (c) Optical micrograph of a sample placed on the bottom diamond of the diamond anvil cell patterned with the Ti/Pt/Au trilayer. The four metallic contacts of the sample (visible through the translucent substrate) touch the four electrodes of the diamond tip. (d) Sketch of the diamond-anvil cell setup. The gasket hole has a diameter of $0.85\text{--}0.9 \text{ mm}$. Ti/Pt/Au electrodes evaporated on the lower diamond serve as leads to contact the sample.

measurements. Measurements were carried out in the van der Pauw configuration with lead permutations, and in a Hall bar configuration. Measurement currents were $1\text{--}5 \mu\text{A}$ at room temperature and $10 \mu\text{A}$ at low temperature for both the van der Pauw samples and the Hall bridges. The power dissipated at the current leads was less than $2 \mu\text{W}$. Carrier density values were extracted from the Hall signals taken with decreasing and increasing temperature. For the diamond-anvil-cell measurements, the pressure was increased in steps of $\sim 0.2 \text{ GPa}$, followed by a 1-2 h waiting time for the pressure and its effects to become steady. Temperature, pressure, and resistance were constantly monitored to follow the stabilization process, which we found to depend on the size of the pressure change and on the sample. For the piston-cylinder-cell measurements, the pressure was increased at room temperature with an oil press in steps of $\sim 2 \text{ MPa}$. The pressure was monitored via the resistance change of a manganin wire inside the sample chamber. At the desired pressure values, the piston cylinder cell was mounted in a physical properties measurement system (PPMS by Quantum Design) for the transport measurements.

B. First principles calculations

To study the n-type $\text{LaAlO}_3\text{--SrTiO}_3$ (001) interface in the thin film geometry, we constructed $(\text{LaAlO}_3)_n/(\text{SrTiO}_3)_m/(\text{LaAlO}_3)_n$ supercells with two symmetric TiO_2/LaO -terminated interfaces and different number of oxide unit cells along the [001] axis ($n = 3\text{--}6$ and $m = 8.5, 20.5$) and (1×1) in-plane dimensions. Calculations for $(\sqrt{2} \times \sqrt{2})$ in-plane dimensions were also performed for some test cases. The case of $n = 5$ and $m = 8.5$ is presented in Fig. 3(a) where half of the supercell is depicted. The other half is obtained using the mirror symmetry with respect to the center of the SrTiO_3 slab (mirror plane). We considered the stoichiometric case with no defects or vacancies. A vacuum layer of more than 25 \AA was inserted to prevent any spurious interactions between the periodic images as in previous slabs calculations.^{23,24} The imposed mirror symmetry of the supercell reduces the effect of a build-up dipole due to the formation of the 2DES at both interfaces. $P = 0$ internal coordinates and lattice vector relaxations were done using a Γ -centered $(8 \times 8 \times 1)$ Monkhorst-Pack \mathbf{k} -mesh which provided atomic positions converged within $1.5 \times 10^{-3} \text{ \AA}$. Ionic forces in the relaxed structures were less than 25 meV/\AA .

Electronic properties of this system were calculated using density functional theory and projector-augmented wave basis²⁵ as implemented in VASP.^{26,27} Electronic wavefunctions were expanded into plane waves up to the cutoff energy of 450 eV . The generalized-gradient approximation²⁸ to the exchange-correlation energy was applied in combination with the GGA+ U scheme²⁹ to treat electronic correlations for strongly localized $3d$ and $4f$ states. For this purpose, we chose $U_{\text{eff}} = 4 \text{ eV}$ for the Ti $3d$ and $U_{\text{eff}} = 8 \text{ eV}$ for the La $4f$ orbitals, which is consistent with the values often stated in the literature. The latter values were used in order to place the La $4f$ empty orbitals at the correct energies.³⁰ The electronic density of states was calculated using the tetrahedron method³¹ on a finer $(16 \times 16 \times 2)$ mesh. Layer-resolved local carrier densities are calculated by integrating the site-projected densities of states in each oxide layer.

III. ZERO-PRESSURE SIMULATIONS

Since the 2DES is extremely sensitive to lattice relaxations—a phenomenon seldom discussed in previous works—we first performed structural optimizations at $P = 0$ by relaxing all internal coordinates and the lattice vectors. The angles between the lattice vectors remain 90° due to the lattice symmetry. For (1×1) in-plane dimensions of the supercell, only displacements along the [001] axis are allowed. We observe that the relaxation procedure reveals a significant reconstruction of the lattice and of the electronic properties already at the level of relaxation of atomic coordinates along [001] only (without volume relaxation), as can be ob-

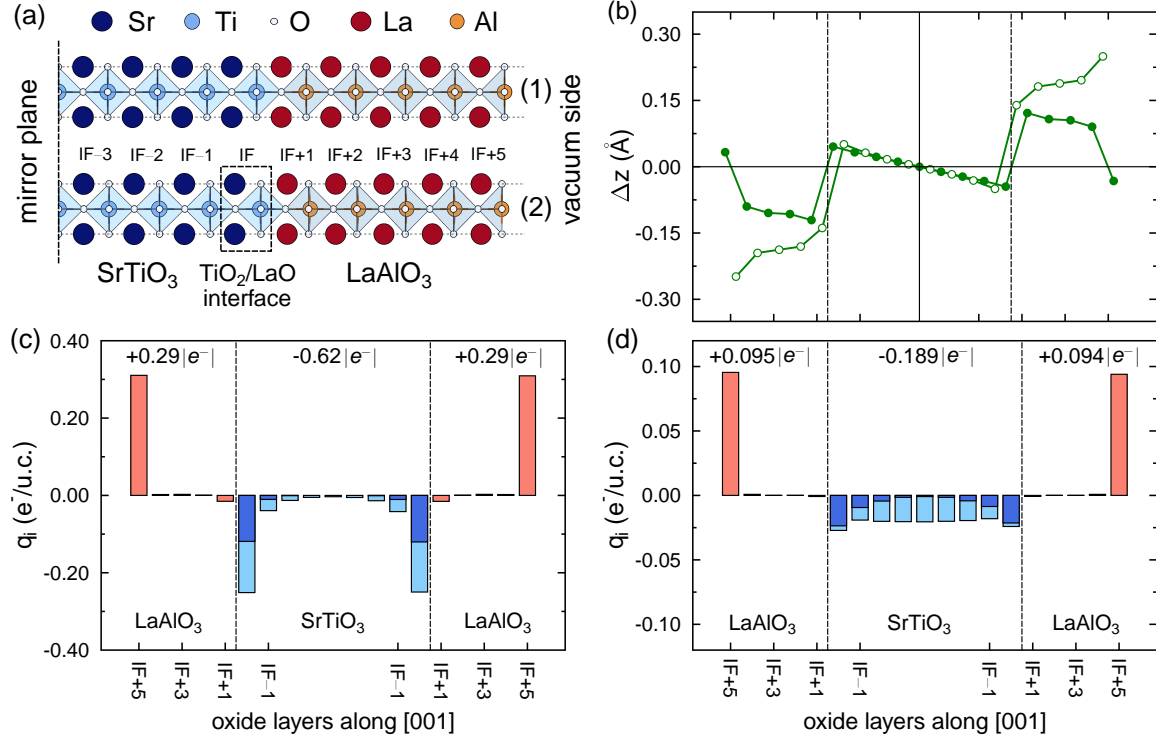


FIG. 3: (a) Half of the $(\text{LaAlO}_3)_n/(\text{SrTiO}_3)_m/(\text{LaAlO}_3)_n$ supercell ($n = 5$, $m = 8.5$) representing the ideal (panel (1)) and fully relaxed (panel (2)) TiO_2/LaO -terminated n-type interface (vacuum side is not fully shown here). The interface unit cell of SrTiO_3 is labeled by IF, and the others by $(\text{IF} \pm 1)$, $(\text{IF} \pm 2)$ etc. Structure figures have been produced with VESTA3.³² (b) Ionic displacements in AO ($A = \text{Sr}, \text{La}$; open symbols) and BO_2 ($B = \text{Ti}, \text{Al}$; filled symbols) oxide layers of the $(\text{LaAlO}_3)_5/(\text{SrTiO}_3)_{8.5}/(\text{LaAlO}_3)_5$ slab relaxed internally with fixed $a_\perp = 3.905$ Å. Positive values on the right of the figure correspond to La and Al cations shifting above the oxygen ions, i.e. closer to the vacuum on the corresponding side of the slab. Due to the imposed mirror symmetry of the supercell, the ionic displacements on the left side of the structure have the opposite signs compared to the right side. (c,d) Unit-cell resolved charge distribution in the $(\text{LaAlO}_3)_5/(\text{SrTiO}_3)_{8.5}/(\text{LaAlO}_3)_5$ slab for the (c) unrelaxed and (d) internally relaxed structures with $a_\perp = 3.905$ Å. Each bar on the plots represents an oxide layer unit cell. “Negative” values correspond to n-type carriers (electrons in the conduction band of SrTiO_3) and “positive” values to p-type carriers (holes in the valence band of LaAlO_3). In the SrTiO_3 film, the darker blue bars show the contribution of the d_{xy} states, compared to the total local charge (light-blue bars). The charge summed over all layers of SrTiO_3 and both LaAlO_3 films is indicated on top of each panel.

served in Fig. 3(b,d). These figures show results for the $(\text{LaAlO}_3)_n/(\text{SrTiO}_3)_m/(\text{LaAlO}_3)_n$ supercell ($n = 5$, $m = 8.5$) with fixed in-plane lattice parameter $a_\perp = 3.905$ Å.

The unrelaxed slab displays a 2DES strongly localized at the interface (Fig. 3(c)), showing almost equal occupations of Ti d_{xy} and d_{xz}/d_{yz} orbitals. Their carrier density is large, approximately $0.3 e^-/\text{u.c.}$. Optimization of the internal atomic positions changes this picture drastically (Fig. 3(d)). The observed shift of electronic states in LaAlO_3 becomes smaller, 0.35 eV per unit cell (Fig. 15(b)). Simultaneously, the charge density at the interface is considerably reduced to $0.1 e^-/\text{u.c.}$, much less than the expected charge transfer of $0.5 e^-/\text{u.c.}$ according to the polar catastrophe picture in its most simplified version. As a matter of fact, there is a large amount of both theoretical and experimental studies in the literature that argue about the origin of this discrepancy (for

a review, see Ref. 33). Possible explanations include vacancy formation, cation disorder and lattice reconstruction. In this paper, we report mainly on this last mechanism, especially in view of our experimental findings regarding pressure effects where we find similar carrier densities $\sim 0.1\text{--}0.2 e^-/\text{u.c.}$ for the 2DES, also under pressure. We also find that after relaxation, the LaAlO_3 film becomes distorted compared to the perfect cubic structure, and adopts a tetragonal symmetry, in agreement with previous studies.^{34,35} This happens because of the lattice mismatch between LaAlO_3 and SrTiO_3 which creates, already at ambient pressure, a strong tensile strain in the LaAlO_3 film. More importantly, positively charged ions (La and Al) are shifted by $\approx 0.2\text{--}0.3$ Å relative to the negative oxygen ions which is reminiscent of a typical displacive ferroelectric transition. The same picture holds for the SrTiO_3 substrate where the displacements Δz , defined as $\Delta z = z_{\text{cation}} - z_{\text{oxygen}}$, have the opposite

direction and a much lower value. The distribution of the ionic displacements in the whole heterostructure is shown in Fig. 3(b) (see Fig. 1(b) for a sketch of the interface).

In general, such a reconstruction pattern screens the interface charge that builds the 2DES. This can be concluded from the sign of the Δz in LaAlO_3 and SrTiO_3 (see Fig. 3(b)). In the LaAlO_3 film, the dipole moment related to the ionic displacements creates a depolarizing electric field directed towards the interface, the same as in the SrTiO_3 substrate. This pushes electrons away from the interface and reduces the accumulated charge. How this becomes important in the case of non-zero external pressure will be discussed further below.

Strictly speaking, the aforementioned internally relaxed structure does not exactly simulate the zero-pressure case because of the mismatch between the theoretical and experimental values of the in-plane lattice parameter. In view of the sensitivity of the electronic structure to the possible lattice and atomic reconstructions, we fully relaxed both the lattice vectors and the internal coordinates which leads to a change of the in-plane lattice parameter a_{\perp} from 3.905 Å to 3.891 Å.⁵³ This slight contraction of the lattice causes only a small reduction of the 2DES density. The orbital character and the overall localization of the relevant states remain unchanged. The main features of the metal-insulator transition in this system vs. the LaAlO_3 thickness are the same for the internally and fully relaxed slabs (Fig. 16). These simulations reproduce the formation of the 2DES starting from 4 LaAlO_3 unit cells. Above the critical thickness, the 2DES density grows continuously with the thickness of the LaAlO_3 film, in agreement with the polar catastrophe scenario. We also investigated the effect of oxygen octahedra tiltings using supercells with $\sqrt{2} \times \sqrt{2}$ in-plane dimensions. Fully relaxed $\sqrt{2} \times \sqrt{2}$ structures with 3 and 5 unit cells of LaAlO_3 were compared at zero pressure to the structures without tilting. These simulations show

that the LAO/STO interface with 3 LaAlO_3 u.c. remains insulating in the presence of octahedra tiltings and the heterostructure with 5 LaAlO_3 u.c. is metallic as before.

One last note regarding the $P = 0$ results is that the lattice reconstruction enhances the weight of the d_{xy} states at the interface and that of the d_{xz}/d_{yz} states towards the middle of the SrTiO_3 slab. This leads to a delocalization of the 2DES which spans the whole SrTiO_3 film with 8.5 u.c. (Fig. 3). Considering larger slabs with 20.5 u.c. of SrTiO_3 (Fig. 4) clearly reduces the occupation of the Ti d_{xz}/d_{yz} orbitals in the middle of SrTiO_3 . The 2DES at the interface is again composed mainly of the Ti d_{xy} orbitals. Our results indicate that at least 7 u.c. of SrTiO_3 on each side of the heterostructure are necessary to accommodate the quasi-2D electronic states and, at the same time, leave a bulk-like region in SrTiO_3 . The same applies to the structural distortions, which decay in SrTiO_3 towards the middle of the slab (Fig. 17), but, in general, show similar features observed in the smaller slabs. In addition, the fully relaxed heterostructure with 20.5 SrTiO_3 u.c. has a larger in-plane lattice constant (3.92 Å) than the slab with only 8.5 SrTiO_3 u.c. (3.89 Å). This shows that the in-plane lattice parameter in these simulations would approach the theoretical estimate for the bulk material (3.94 Å in Ref. 36) in the limit of a very thick SrTiO_3 film. More importantly, we find that the integrated charge of the slab with 20.5 u.c. of SrTiO_3 is already well reproduced by the smaller supercell with 8.5 u.c. of SrTiO_3 . This gives us confidence in performing the pressure simulations with the computationally less costly smaller slabs.

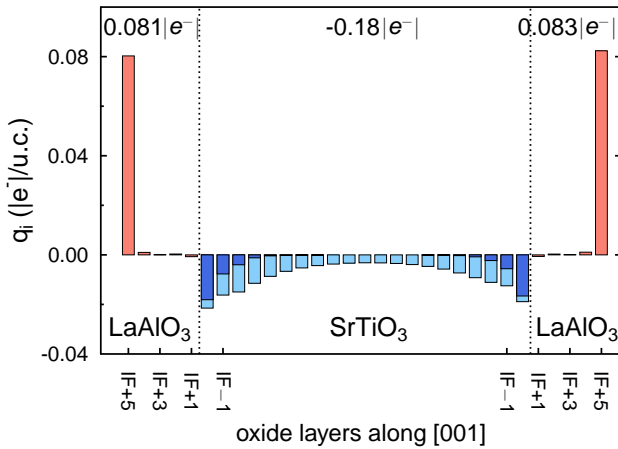


FIG. 4: Charge distribution in the fully relaxed $(\text{LaAlO}_3)_5/(\text{SrTiO}_3)_{20.5}/(\text{LaAlO}_3)_5$ slab at zero pressure. Contribution of the d_{xy} states is shown by the dark-blue bars.

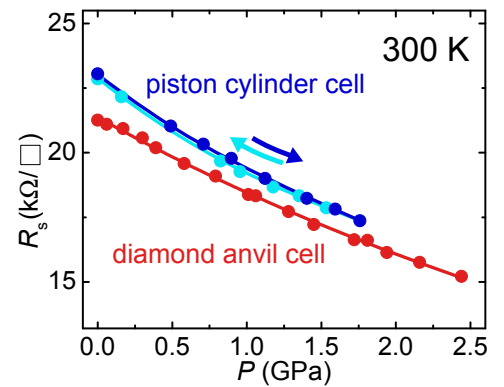


FIG. 5: Sheet resistance of the 2DES in a LaAlO_3 - SrTiO_3 heterostructure measured at room temperature as a function of pressure. The LaAlO_3 layer of these samples is 5 u.c. thick. Lines serve as a guide to the eye. Experimental errors fall within the symbol size.

IV. EFFECT OF PRESSURE

A. Experimental results

The effect of P on the room temperature (RT) conductivity of the 2DES at the interface between LaAlO_3 and SrTiO_3 is shown in Fig. 5. Pressure produces a smooth decrease in the sheet resistance of the 2DES, which amounts to $\sim 30\%$ for the maximum 2.44 GPa achieved in the diamond anvil cell setup. The pressure-induced monotonous and smooth resistance decrease at room temperature ($\sim 14\%$ at 1 GPa) was shown by all samples (~ 10). As shown in Fig. 5, the change of resistance with pressure is a reversible process. Also, cycling to 4 K under pressure was not found to cause irreversibilities. The observed reversibility and reproducibility indicate that we measure the intrinsic response of the 2DES to P . The decrease in resistance upon increasing P at RT hints at a decrease of the electron-phonon scattering caused by pressure-induced phonon hardening. To unravel the effects of pressure on the intrinsic electronic properties of the interface we measured the effects of hydrostatic pressure on the 2DES at low temperatures. For clarity, we focus in the following discussion on the behavior at the lowest temperature used, 4 K, and examine the room-temperature behavior in the Supplement (see Fig. 18).

Whereas the sample resistance decreases with pressure at 300 K, hydrostatic pressure increases the resistance slightly at low temperatures (Fig. 6(a)). Multiple samples consistently exhibit this increase in sheet resistance at 4 K, both in van der Pauw and Hall bar configurations. The extent of the increase of resistance at 4 K, however, can vary, presumably depending on the quality of the sample (see the Supplement Fig. 19 and Fig. 20 for more details). The increase of the sample resistance goes hand in hand with a reversible doubling of the sheet carrier density n_s (Fig. 6(b)). As a side note it is worth mentioning that magnetic field sweeps beyond ± 3 T reveal in this magnetic field range an obvious multiband behavior consistent with the high carrier density shown by these samples and in agreement with other studies.³⁷ At smaller fields the characteristics are pronouncedly more linear (Fig. 21 in the Supplement). The trend observed under P is nevertheless captured by the simplified one-band analysis shown in this work.⁵⁴ The measured increase of n_s is compensated by a large pressure-induced reduction of the mobility μ (Fig. 6(c)). Interestingly, a comparable relation between n_s and μ was revealed in a study by Y. Xie and coworkers.³⁸ In that work, modifications of the LaAlO_3 surface led to an inverse proportionality between n_s and μ . Recent pressure experiments by D. Fuchs *et al.* in LaAlO_3 - SrTiO_3 bilayers provide evidence of a similar response of the carrier density and mobility to hydrostatic pressure.²⁰ Note, however, that the sample from Ref. 20, grown at lower temperatures and oxygen partial pressures, is intrinsically different to the ones investigated here. With a LaAlO_3 layer five

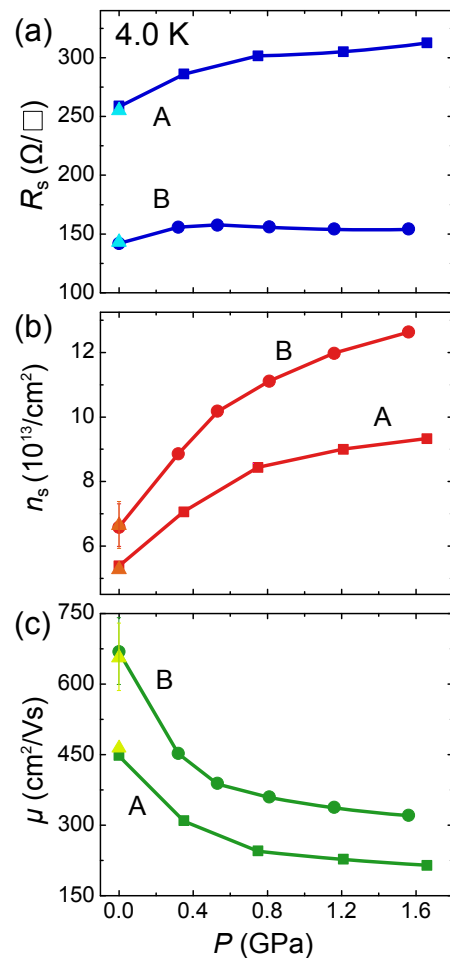


FIG. 6: Measured transport properties of the LaAlO_3 - SrTiO_3 2DES as a function of hydrostatic pressure. (a) Sheet resistance, (b) sheet carrier density and (c) carrier mobility of two LaAlO_3 - SrTiO_3 heterostructures measured at 4 K as a function of applied pressure. Sample A (5 u.c. thick LaAlO_3) was measured in a van der Pauw geometry, sample B (6 u.c. thick LaAlO_3) by using a Hall bridge. Triangles show data taken after unloading the cell. Lines serve to guide the eye. For clarity, only those error bars that exceed the bullet size are drawn. The corresponding properties of the samples measured at room temperature are recorded in the Supplement.

times thinner, our samples are twice as conducting and have a larger carrier density at ambient pressure.

In order to clarify the mechanism behind the drastic changes of the 2DES observed in our experiment, we proceed in what follows with our *ab initio* DFT-based theoretical investigation.

B. Results of the simulations

Starting from the fully relaxed structure with $a_{\perp} = 3.891$ Å, which corresponds, in our calculations, to zero external pressure,⁵⁵ we investigate the effects of hydrostatic pressure by scaling down the lattice vectors by a

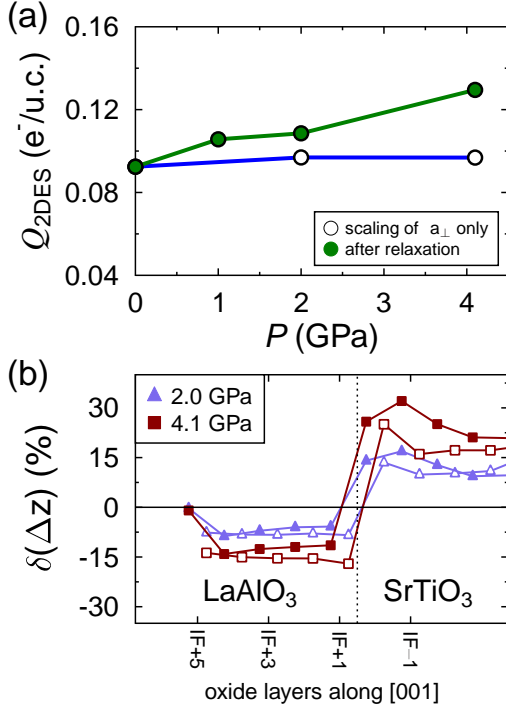


FIG. 7: (a) Calculated 2DES density vs. applied hydrostatic pressure for 5 LaAlO_3 unit cells. Open symbols represent the results of scaling-only simulations of pressure, and filled symbols demonstrate the effect of the additional internal relaxation under pressure. (b) Relative change of the ionic displacements $\delta(\Delta z) = (\Delta z' - \Delta z)/\Delta z \times 100\%$ in different layers of the fully relaxed $(\text{LaAlO}_3)_5/(\text{SrTiO}_3)_{8.5}/(\text{LaAlO}_3)_5$ heterostructure (only half of the cell is shown) in response to hydrostatic pressure; open symbols represent the AO layers and filled symbols – the BO_2 layers; $\Delta z'$ stands for ionic displacements at the considered pressure ($P \neq 0$), Δz corresponds to zero pressure.

certain percentage $\delta = \Delta a_\perp/a_\perp \times 100\%$ and we first keep fixed the internal atomic positions. Values of δ equal to 0.5% and 1.0% correspond to the application of an isotropic pressure of $P = 2.0$ GPa and $P = 4.1$ GPa, respectively, as determined from the *ab initio* stress tensor. This simple procedure does not reveal any changes in the 2DES distribution and density as a function of pressure, as depicted in Fig. 7(a) (empty symbols). We then perform a further relaxation of internal coordinates (keeping fixed the AlO_2 surface layers positions⁵⁶) in order to describe possible lattice reconstructions under applied pressure. Our results indicate that this additional relaxation has a large impact on the 2DES density (Fig. 7(a) (full symbols)). First of all, it leads to sizable changes of the ionic displacements in both materials as presented in Fig. 7(b) where the relative change of the ions displacements $\delta(\Delta z) = (\Delta z' - \Delta z)/\Delta z \times 100\%$, ($\Delta z'$ stands for ionic displacements at the considered pressure ($P \neq 0$), and Δz corresponds to zero pressure) is shown for two representative pressure values of 2.0 GPa and 4.1 GPa. Lattice distortions in LaAlO_3 are reduced by 15% for the

largest studied pressure, whereas they increase in SrTiO_3 by more than 25% (a sketch of this effect is also shown in Fig. 1). It should be mentioned here that the ionic displacements in SrTiO_3 are much smaller than those in LaAlO_3 (see Fig. 3(b)). The observed structural changes are accompanied by an enhancement of the integrated interface charge, localized in the SrTiO_3 portion, from 0.09 $e^-/\text{u.c.}$ for 0 GPa to 0.13 $e^-/\text{u.c.}$ for 4.1 GPa,⁵⁷ i.e. by approximately 45% (see Fig. 7(a)). The charge increases almost linearly as a function of the applied pressure, although there is apparently a plateau near 1 GPa which compares well with the saturation region for the experimental curve on Fig. 6. The characteristic charge distribution, shown in Figure 3(d) for the zero-pressure case, does not change qualitatively for larger pressures. The n-type charge carriers in this slab are distributed over the whole SrTiO_3 film, and p-type charges with the same total density are localized within a few atomic layers near both LaAlO_3 free surfaces. For each value of pressure, 85% of the local 2DES charge on the interfacial Ti cations is accommodated by the d_{xy} orbitals. The situation is opposite far from the interface, where the d_{xz}/d_{yz} states dominate. Summed over all SrTiO_3 layers, the total charge of the 2DES contains around 35% d_{xy} character and the rest has d_{xz}/d_{yz} character. Under pressure, the charge densities of both the d_{xy} interface states and the d_{xz}/d_{yz} states (in-depth propagating into the bulk part of SrTiO_3) increase (Fig. 8), giving rise to the aforementioned overall enhancement of the 2DES carrier concentration by 45%. The layer- and orbital-resolved charge profiles for the thicker slab with 20.5 STO u.c. at zero pressure and $P = 2.1$ GPa are shown in Fig. 22.

Analyzing the curvature of the light d_{xy} and heavy d_{xz}/d_{yz} bands near the Γ point of the Brillouin zone (Fig. 9) we determine the effective electron masses in units of the electron rest mass (m^*/m_e). At zero pressure, m^*/m_e for the light and heavy bands are 0.46 and

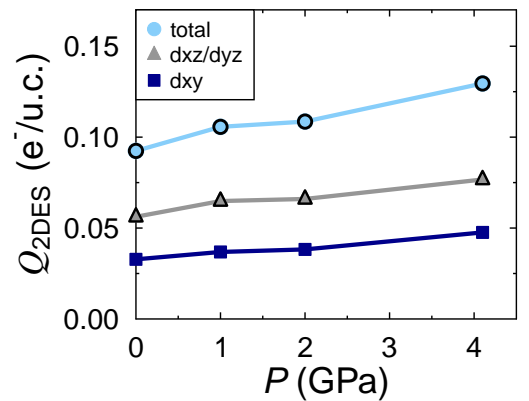


FIG. 8: Orbital-resolved 2DES charge density vs. applied pressure. Similar to Fig. 7(a), the effect of the additional lattice reconstruction under pressure is included here. The charge density represents the sum over all SrTiO_3 layers.

4.17 while at 4.1 GPa, the values are 0.44 and 3.88 respectively. These results would suggest a slight enhancement of the mobility of the 2DES charge carriers, which contradicts, however, the low-temperature experimental observations in the present work. In the following, we will try to resolve this puzzle by analyzing the polarization in LaAlO_3 as well as the dielectric response in LaAlO_3 and SrTiO_3 as a function of pressure.

1. Polarization in LaAlO_3

We performed a Berry phase analysis⁴⁰ of the electronic polarization of selected structures which, together with the ionic contribution, describe the response of LaAlO_3 to the interface polarity and strain conditions.

In order to estimate the polarity within the relaxed LaAlO_3 - SrTiO_3 heterostructure, we cut the third unit cell of LaAlO_3 away from the interface (IF+3) out of the slab and form an artificial new bulk material (Fig. 10) with the distortion of the heterostructure. Important

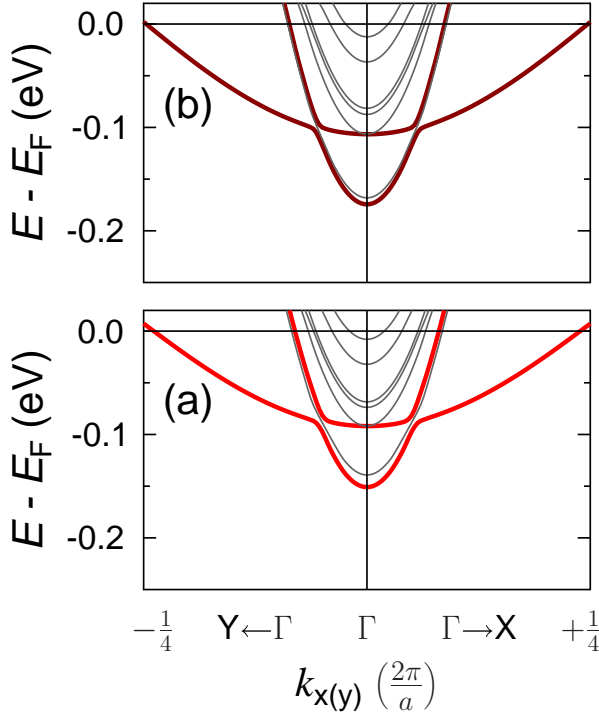


FIG. 9: Band structure of the n-type LaAlO_3 - SrTiO_3 heterostructure for the (a) zero-pressure case and (b) $P = 4.1$ GPa. The lowest occupied Ti d conduction bands are indicated by the thick lines, whereas the background band structure is plotted using thin gray lines. The lowest light band has the largest weight on the interfacial Ti d_{xy} states, while the single heavy band has contributions from all TiO_2 oxide layers and is composed mainly of the d_{xz}/d_{yz} states of the more distant Ti sites. The site-resolved analysis of bands was performed using the *PyProcar* code.³⁹

features, captured by this artificial bulk LaAlO_3 , are the tetragonal distortion along the $[001]$ direction as well as the La-O and Al-O ionic displacements. The latter are zero in the normal bulk LaAlO_3 and can be stabilized only in the heterostructure. These structural features are similar for all LaAlO_3 unit cells along the growth direction, so we consider the newly constructed artificial bulk as representative of the whole LaAlO_3 film.

Both in LaO and AlO_2 atomic planes, the displacements between cations and oxygen atoms are positive along the $[001]$ axis (Fig. 10) oriented away from the interface. In order to calculate the dipole moment of this system, we define a centrosymmetric counterpart with the same lattice vectors where all displacements are zero. Starting from this high-symmetry phase, one can gradually approach the low-symmetry phase through linear interpolation of atomic coordinates (see, for example, Ref. 41). The energy profile calculated along the deformation path (Fig. 10(b)) indicates that the low-symmetry phase is unstable in the bulk since the high-symmetry phase is 80 meV/u.c. lower in energy. However, for each intermediate structure, one can estimate the electric dipole moment and, therefore, determine the total change of polarization along the aforementioned path. The latter value is taken as the polarization of the distorted LaAlO_3 structure.

Using this procedure, we find that both ionic and electronic contributions are non-vanishing in the studied case. For the LaAlO_3 cell taken from the fully relaxed heterostructure with $n = 5$ LaAlO_3 layers and at two pressures (2.0 and 4.1 GPa), the total values of the lattice polarization are presented in Table I, compared to the zero-pressure case. The observed decrease of the lattice polarization for larger pressures is consistent with a considerable suppression of lattice distortions (Fig. 7(b)). In general, the polarization is oriented towards the free LaAlO_3 surface, which means that it partially screens the interface charge. This explains why the observed densities of the 2DES at $P = 0$ are almost an order of magnitude smaller than the value of $0.5 e^-/\text{u.c}$ predicted by the polar catastrophe model. Understandably, the 2DES density becomes larger when the polarization of LaAlO_3

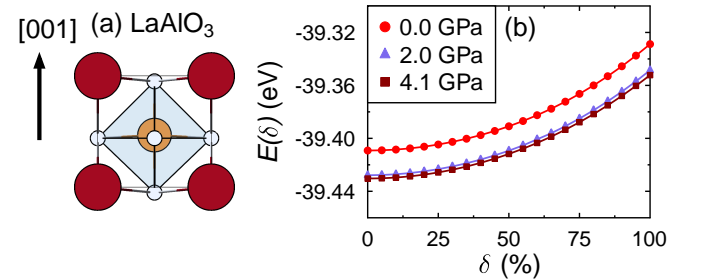


FIG. 10: (a) Unit cell of the distorted LaAlO_3 and (b) the potential profile $E(\delta)$ for the transition between the centrosymmetric ($\delta = 0\%$) and polarized ($\delta = 100\%$) tetragonal phases.

TABLE I: Total lattice polarization p of LaAlO_3 (in units of $\mu\text{C}/\text{cm}^2$ and $e \cdot \text{\AA}$) and the interface charge density σ calculated as functions of the hydrostatic pressure applied on the LaAlO_3 - SrTiO_3 system with 5 u.c. of LaAlO_3

P (GPa)	p ($\mu\text{C}/\text{cm}^2$)	p ($e \cdot \text{\AA}$)	σ ($e^-/\text{u.c.}$)
0	34.5	1.22	0.09
2.0	31.5	1.12	0.11
4.1	30.1	1.04	0.13

and, therefore, the lattice screening are reduced under pressure. If the lattice distortions were not present, then the screening would be close to zero and the interface charge Q would approach its maximal value of $0.5 e^-$, as expected from the polar catastrophe scenario in its simplest version and confirmed by the large carrier density obtained in our calculations for the unrelaxed heterostructures (Fig. 3(c)). In reality, however, the finite thickness of LaAlO_3 together with structural relaxation effects lead to a non-vanishing induced lattice polarization. We expect our *ab initio* data for this polarization to better agree with our measurements, which were done in the absence of photo-illumination, since the latter induces additional carriers that screen the polar discontinuity and suppress the LaAlO_3 polarization as well as the internal field, as found in Refs. 42 and 43.

In view of the above discussion, one can reconsider the effect of the GGA+ U corrections on the lattice reconstruction and electronic properties of the 2DES. In particular, we find a substantial increase by more than 200% of the carrier density as the U_{eff} parameter on the La 4*f* states varies between 0 and 8 eV (results not shown here). The origin of this strong dependence can be found in the structural features. Intralayer displacements in LaAlO_3 are moderately suppressed for $U_{\text{eff}}(\text{La}) = 8$ eV, which, according to the previous discussion, effectively reduces the screening of the polar discontinuity and enhances the charge density at the interface.

2. Dielectric properties

The dielectric response, both from the lattice and from the electronic subsystems, was obtained using the formalism described in Refs. 44 and 45.

Whereas the behavior of the lattice polarization in LaAlO_3 under pressure explains the experimental trends of the 2DES density, another mystery remains to be solved. Experimentally, we find that the interface resistivity increases as a function of pressure, although the carrier density becomes larger. This implies that the mobility of the electron system is significantly reduced. However, at the beginning of this section we have seen that the observed changes in the band structure under pressure cannot explain this reduction. In searching for an explanation to this puzzle, we turn our attention

to the pressure-dependent dielectric permittivity of the LaAlO_3 and SrTiO_3 portions of the studied heterostructure, which are arguably different from their bulk counterparts. The dielectric properties have an impact on the screening of charged impurities and therefore affect the sample conductivity.

In the first step, we study the dielectric response of the distorted “bulk” LaAlO_3 , in view of the polarization effects discussed above. One has to distinguish between the contribution of the lattice ($\varepsilon_{\text{ion}}(\omega)$) to the complex permittivity $\varepsilon(\omega)$, which prevails at low frequencies, and the electronic dielectric constant $\varepsilon_{\text{el}}(\omega)$, which shows oscillations at higher frequencies, usually in the THz region. Our results indicate that the electronic tensor $\varepsilon_{\text{el}}(\omega)$ is diagonal with slightly different in-plane and out-of-plane components due to the tetragonal distortions in the LaAlO_3 . The effect of increasing pressure is almost negligible for $\varepsilon_{\text{el}}(\omega)$ (not shown here): characteristic peaks shift only slightly towards higher frequencies, and the static permittivity reveals almost no dependence on pressure.

A larger effect can be expected from the lattice response of LaAlO_3 , which is well known to give the largest contribution to the static dielectric permittivity.⁴⁴ It can be determined from the vibrational modes and Born effective charges. Due to the epitaxial strain, the dielectric permittivity is an anisotropic tensor, which turns out, however, to be diagonal, similar to $\varepsilon_{\text{el}}(\omega)$. The anisotropy makes the in-plane components $\varepsilon_{x,y}$ larger and the out-of-plane component ε_z smaller than the bulk value (28.7 in our calculations for the equilibrium lattice volume). Our findings reveal a large pressure-induced reduction of all components of the ionic dielectric tensor, in contrast to the electronic counterpart, which shows almost no changes. At the end, this gives a sizable suppression of the total static permittivity tensor with applied pressure (see Fig. 11). The in-plane components $\varepsilon_{x,y}$ are

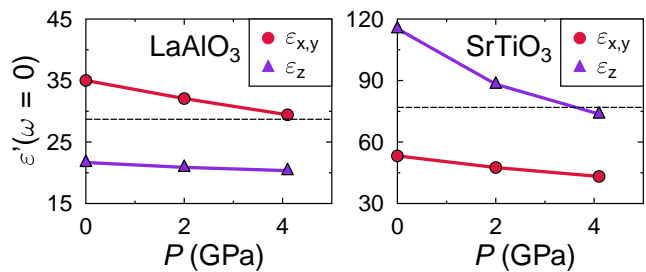


FIG. 11: Pressure dependence of the static dielectric permittivity $\varepsilon'(\omega = 0)$ (real part) of LaAlO_3 and SrTiO_3 . In each case, the structure is taken from the middle unit cell of the corresponding material in the fully relaxed $(\text{LaAlO}_3)_5/(\text{SrTiO}_3)_{8.5}/(\text{LaAlO}_3)_5$ slab, shown in Fig. 3(a). The values of ε' for bulk oxides with their native cubic structure are negligible and are, therefore, not presented here. In each panel, the lines connecting points on the plot are guides to the eye.

most affected in this process, and the out-of-plane component ϵ_z remains practically constant, i.e. the LaAlO_3 oxide becomes dielectrically more isotropic with growing pressure, which must be due to the suppressed ionic displacements.

We perform an analogous study for the SrTiO_3 substrate. A crucial difference, however, is the electronic structure, which is metallic throughout the whole SrTiO_3 layer in the case of 8.5 SrTiO_3 unit cells in the slab. For that reason, if we consider a local cut of its structure, its bulk insulating properties cannot be directly related to those of the heterostructure. Nevertheless, we might consider, in the first approximation, the effect of lattice deformation in SrTiO_3 under pressure on the dielectric tensor, calculated for the insulating bulk phase with a structure taken from the central unit cell of the slab. Due to the mirror symmetry, the intralayer Δz are zero, so that only tetragonal distortions are present. In Fig. 11 (right panel), the calculated out-of-plane component ϵ_z drops rapidly against external pressure, while the in-plane component shows much smaller changes. This is the opposite situation compared to LaAlO_3 , where the in-plane $\epsilon_{x,y}$ showed the largest response to pressure. However, both materials demonstrate a substantial suppression of their dielectric constants as the hydrostatic pressure is applied.

We note that our calculated structures show an almost constant c/a ratio for the studied pressure range, which means that the SrTiO_3 lattice parameter is simply scaled down with increasing pressure. In this respect, we can compare our results with related experiments⁴⁶ on bulk SrTiO_3 with cubic symmetry, summarized in Fig. 12. These experiments demonstrated a pressure-dependent dielectric constant $\epsilon'(P) = C/(P - P_0)$ that decreases monotonically with pressure, similar to a Curie-Weiss law.

At this point, we can address the issue of reduced mobility of the 2DES. As we discussed previously, due to the suppression of lattice polarization in LaAlO_3 under pressure the screening of the polar discontinuity is reduced. As a result, the density of the interface charge carriers is enhanced. If crystal defects or impurities were present in both parts of the heterostructure, they would serve as scattering centers for the charge carriers from the 2DES. By increasing pressure, we find a clear decrease of the dielectric constants of both LaAlO_3 and SrTiO_3 . This results in a less effective screening of crystal defects by the lattice ions and, consequently, a higher scattering rate for the mobile charge carriers. We argue that this might be the origin of the reduced mobility that leads to an increase in sheet resistivity, as shown in Fig. 6(a,c).

V. CONCLUDING REMARKS

In this paper, we performed a combined experimental and theoretical study of the hydrostatic pressure effects on the electronic properties of the 2DES in LaAlO_3 - SrTiO_3 (001). On the one hand, experimental results

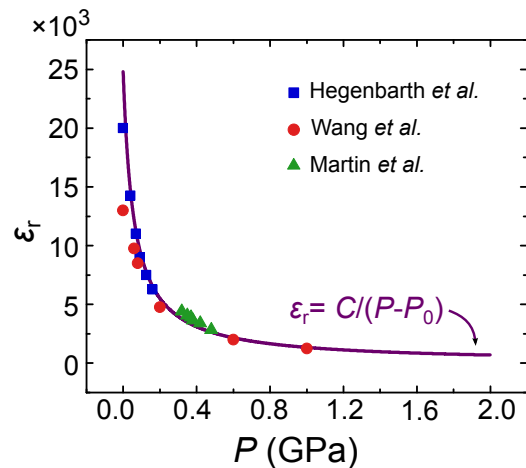


FIG. 12: Measured pressure dependence of low-temperature dc-dielectric constant of SrTiO_3 single crystals as compiled from the literature.^{47–49} The data of reference⁴⁸ were measured at a bias field of 2.5 kV/cm, the other data without a bias field. The original data were taken at temperatures close to 4.2 K, but not necessarily at 4.2 K. If necessary we interpolated or extrapolated the measured data to 4.2 K. The solid line presents a fit to the function $\epsilon_r(P) = C/(P - P_0)$ with $C = 1420 \text{ GPa} \pm 60 \text{ GPa}$ and $P_0 = -0.06 \text{ GPa} \pm 0.01 \text{ GPa}$.

of this work show that the density of the electron system is considerably enhanced by moderate pressures, i.e. by almost 100% at $\sim 1.6 \text{ GPa}$. This phenomenon can be explained by the induced lattice reconstruction of the LaAlO_3 film, which acts against the interface charge and can be partially suppressed by the external pressure, as demonstrated by our first-principle analysis. Other effects by which pressure alters the carrier density cannot be discarded, but our measurements did not give indications of their existence. On the other hand, the calculated static dielectric permittivity decreases under the influence of pressure for both materials (LaAlO_3 and SrTiO_3), which at least partly accounts for the experimental observations of the enhanced interface resistivity.

The interface screening is an orbital-dependent phenomenon: clearly, the d_{xz}/d_{yz} states propagate much further, into deeper layers of SrTiO_3 , whereas the d_{xy} states are more localized within 3–4 u.c. near the interface. Our calculated results with thick slabs indicate that 7 u.c. of SrTiO_3 are involved in the formation of the 2DES. An important issue here is the band gap of both oxides. In our GGA+ U calculations with $U = 4 \text{ eV}$ on the Ti d states, the band gap of bulk SrTiO_3 is estimated to be equal to 2.4 eV, which is closer to the experimental value (3.2 eV) than the standard GGA estimate (1.8 eV). Nevertheless, the delocalization effect might be slightly overestimated in our calculations. This should not affect qualitatively the statements concerning the total electron density changes in response to the external pressure.

Further open issues are, for instance, point defects and their role under high pressures. Recently, polarity-induced defect formation at ambient pressure was dis-

cussed as an alternative origin of the 2DES^{50,51} in order to resolve certain purported shortcomings of the polar catastrophe scenario. It cannot be completely ruled out that, under pressure, these defects produce additional carriers. We believe, however, that our calculations of the ideal LaAlO_3 - SrTiO_3 structure still uncover relevant processes that occur under pressure. Whereas the defect-free LaAlO_3 and SrTiO_3 layers in our study demonstrate large dielectric changes under pressure, which affect both the density and the mobility of the 2DES, it might well happen that the concentration and distribution of defects in both materials are not constant⁵⁸ as well, which would have an important effect on the dielectric response. The observed increase of the 2DES density would be further enhanced when the negatively charged oxygen defects, possibly present at the AlO_2 surface,^{42,52} multiply at higher pressures. Verification of this hypothesis merits further study.

ACKNOWLEDGEMENTS

Part of this work was financially supported by DFG Sonderforschungsbereich TRR 49 and TRR 80, and Research Unit FOR 1346. We would like to thank M. Altmeyer, H. Boschker, M. Lanzano, and U. Zschieschang for many useful discussions. The authors thank U. Engelhardt, A. Güth, I. Hagel, M. Hagel, C. Hughes, Y. Link, M. Schmid, and B. Stuhlhofer for their support, and B. Keimer and R. Kremer for access to the piston cylinder cell and the physical property measurement system. The computer time was allotted by the centre for supercomputing (CSC) in Frankfurt and by the computer center of Goethe University.

Hydrostatic pressure response of an oxide two-dimensional electron system

J. Zabaleta,¹ V.S. Borisov,² R. Wanke,¹ H.O. Jeschke,² S.C. Parks,¹ B. Baum,¹ A. Teker,¹
T. Harada,¹ K. Syassen,¹ T. Kopp,³ N. Pavlenko,³ R. Valentí,² and J. Mannhart¹

¹*Max Planck Institute for Solid State Research, 70569 Stuttgart, Germany*

²*Institute of Theoretical Physics, Goethe University, 60438 Frankfurt am Main, Germany*

³*Center for Electronic Correlations and Magnetism,
University of Augsburg, 86135 Augsburg, Germany*

(Dated: May 30, 2016)

Supplementary Material

In the following section we compile figures of measurements and calculations as supporting information to our work.

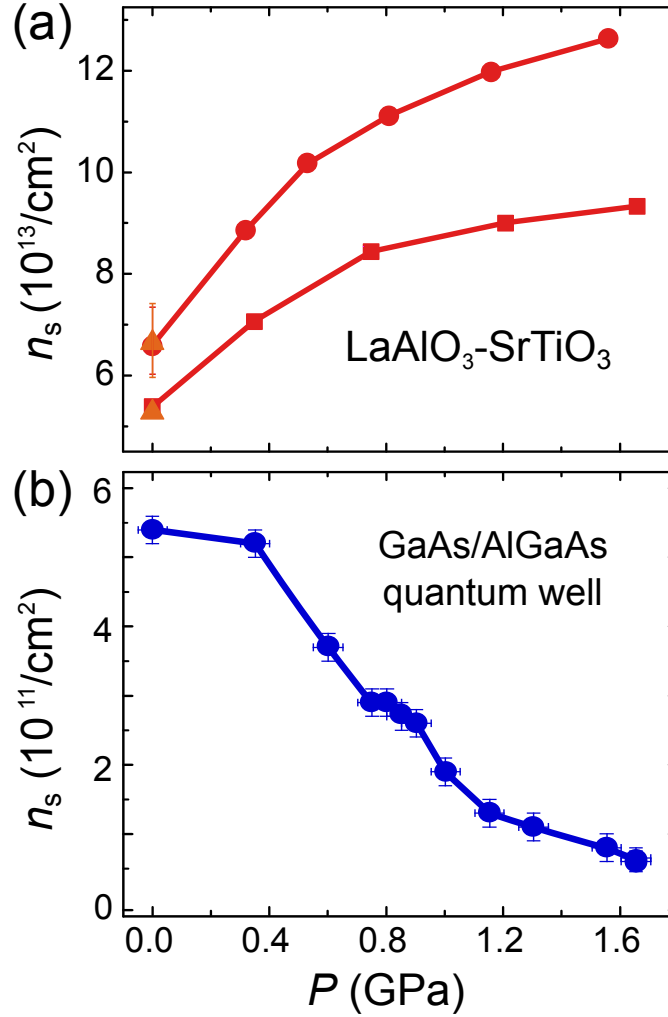
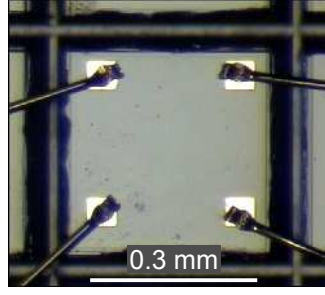


FIG. 13: Effect of pressure on 2D carrier densities: (a) Behavior of the $\text{LaAlO}_3\text{-SrTiO}_3$ interface compared to (b) a GaAs/AlGaAs single quantum well (data redrawn from Ref. 21). Only error bars that exceeded the bullet size are drawn.



T (K)	R_s (k Ω) before cut	R_s (k Ω) after cut	n_s (cm $^{-2}$) after cut	μ (cm 2 /Vs) after cut
300	17	13	1.1×10^{14}	4.7
4	0.150	0.157	3.1×10^{13}	990

FIG. 14: Optical microscopy image of a cut sample wire bonded for electrical characterization, and table of the electrical characterization results of the assembly at ambient pressure.

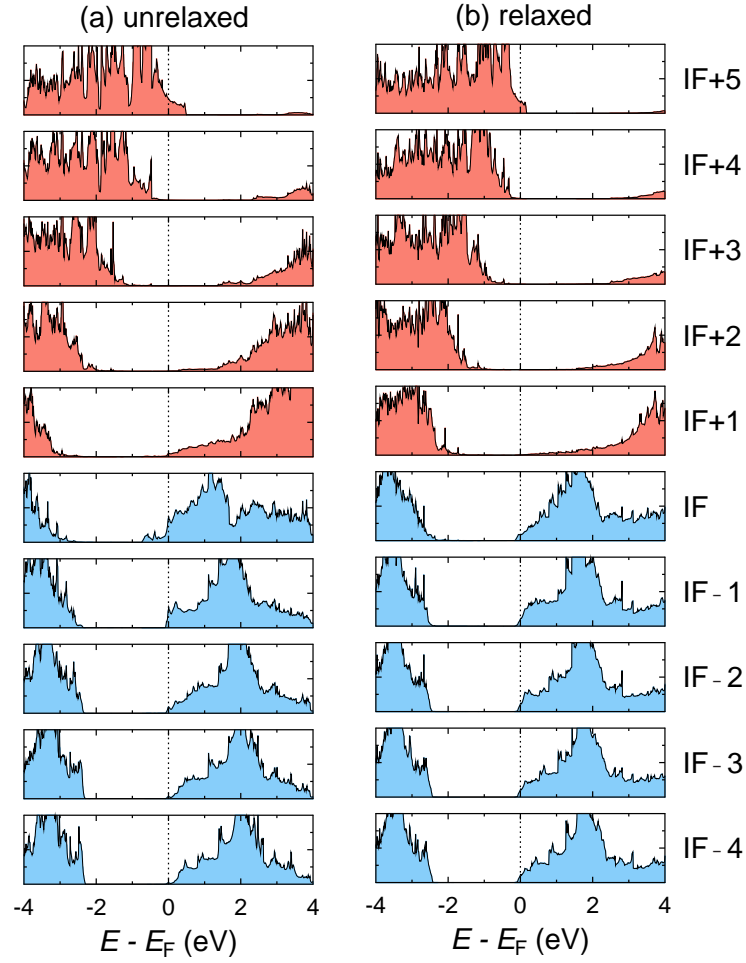


FIG. 15: Unit-cell resolved density of states of the $(\text{LaAlO}_3)_5/(\text{SrTiO}_3)_{8.5}/(\text{LaAlO}_3)_5$ slab for the unrelaxed (left panel) and structures relaxed internally while keeping the in-plane lattice parameter fixed at $a_{\perp} = 3.905 \text{ \AA}$ (right panel). Layers are labeled in the same way as in Fig. 3(a) from the main text.

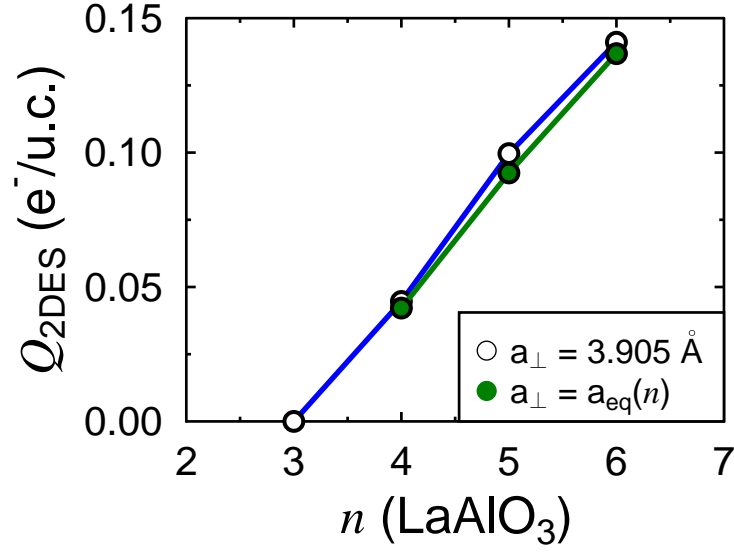


FIG. 16: 2DES density vs. the LaAlO₃ thickness. Filled symbols represent fully relaxed structures with the equilibrium lattice constant a_{eq} being a function of n (number of LaAlO₃ unit cells) and open symbols stand for internally relaxed structures with fixed $a_{\perp} = 3.905$ Å. The lines connecting points on the plot are guides to the eye.

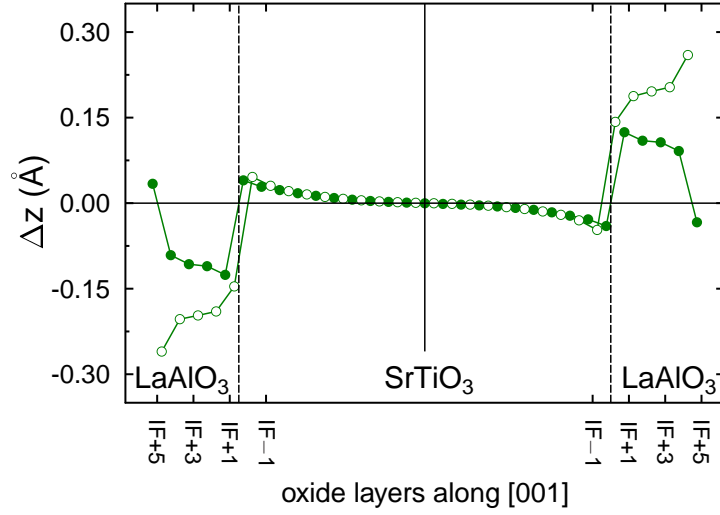


FIG. 17: Ionic displacements in AO ($A = \text{Sr, La}$; open symbols) and BO_2 ($B = \text{Ti, Al}$; filled symbols) oxide layers of the fully relaxed $(\text{LaAlO}_3)_5/(\text{SrTiO}_3)_{20.5}/(\text{LaAlO}_3)_5$ slab at zero pressure.

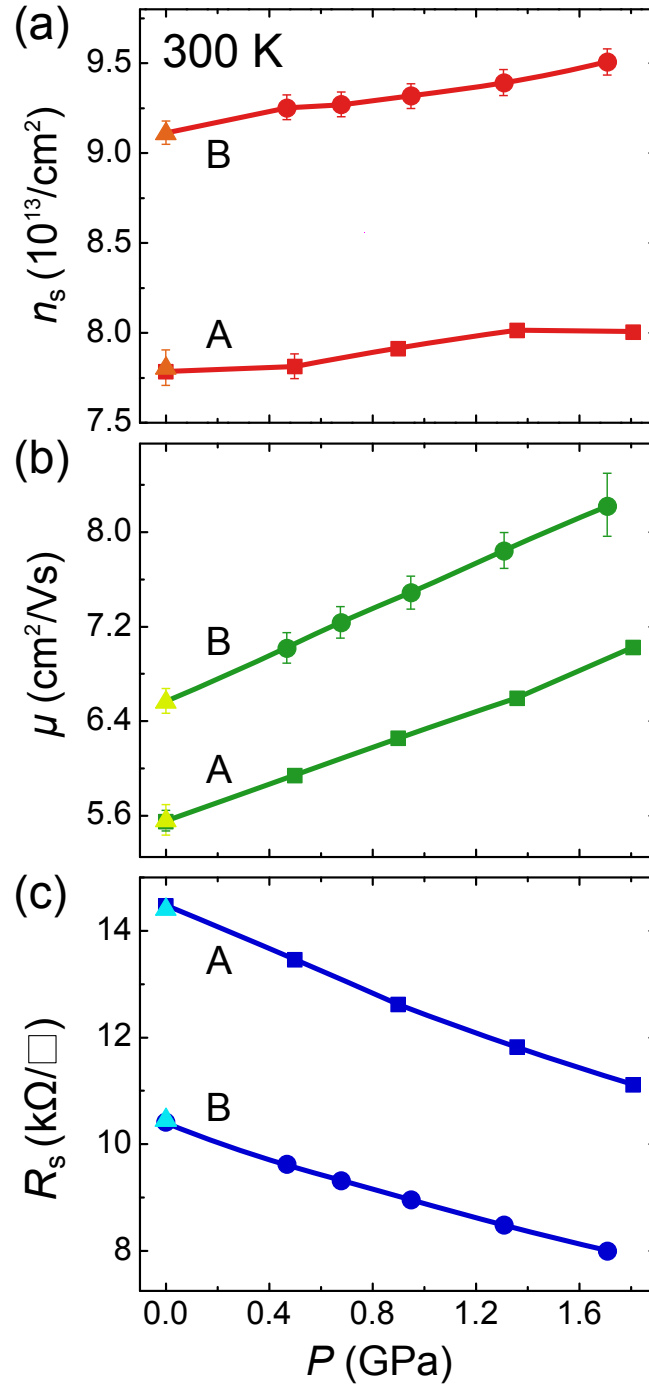


FIG. 18: Transport properties of the LaAlO₃-SrTiO₃ 2DES as a function of hydrostatic pressure measured at room temperature. Sheet carrier density (a), mobility (b), and sheet resistance (c) of van der Pauw and Hall bar samples as a function of applied pressure. Triangles stand for measurements after unloading the cell. For clarity, only those error bars that exceed the bullet size are drawn. Lines serve as guides to the eye.

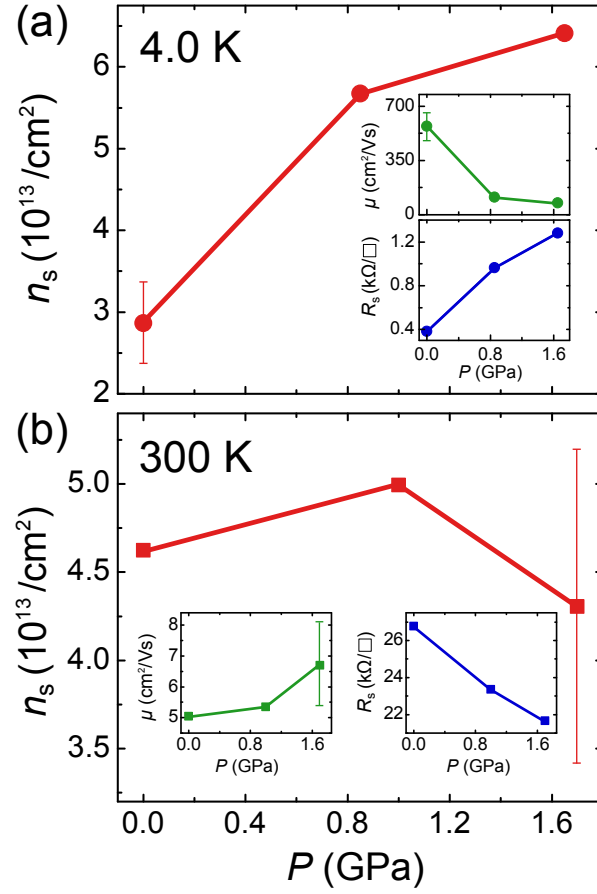


FIG. 19: Transport properties of a $\text{LaAlO}_3\text{-SrTiO}_3$ 2DES in van der Pauw configuration as a function of hydrostatic pressure. This sample showed the largest pressure-induced changes of the sheet carrier density and the carrier mobility at 4 K. The error bars reflect the differences of the results of different magnetic-field sweeps. During the 1.7 GPa warmup a contact deteriorated, resulting in the large error bar of the data point at 300 K, 1.7 GPa. Only error bars that exceed the bullet size are drawn. Lines serve as guides to the eye.

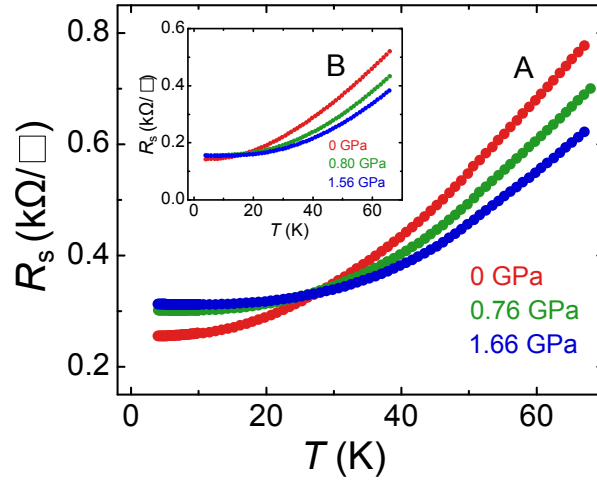


FIG. 20: Sheet resistance of sample A (van der Pauw configuration) and B (Hall bar configuration) measured as a function of temperature for several values of hydrostatic pressure. The two types of samples show similar characteristics.

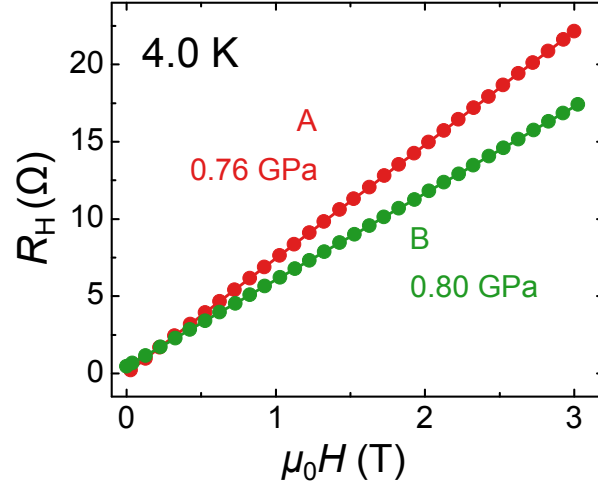


FIG. 21: Hall resistance as a function of the magnetic field measured on two samples (A: 5-unit-cell-thick LaAlO_3 , van der Pauw; B: 6-unit-cell-thick LaAlO_3 , Hall bridge) at 4 K under hydrostatic pressure. In order to exclude longitudinal components in the Hall resistance, the values shown here are anti-symmetrized, e.g. we plot the averaged difference between the Hall resistance measured at identical positive and negative magnetic fields.

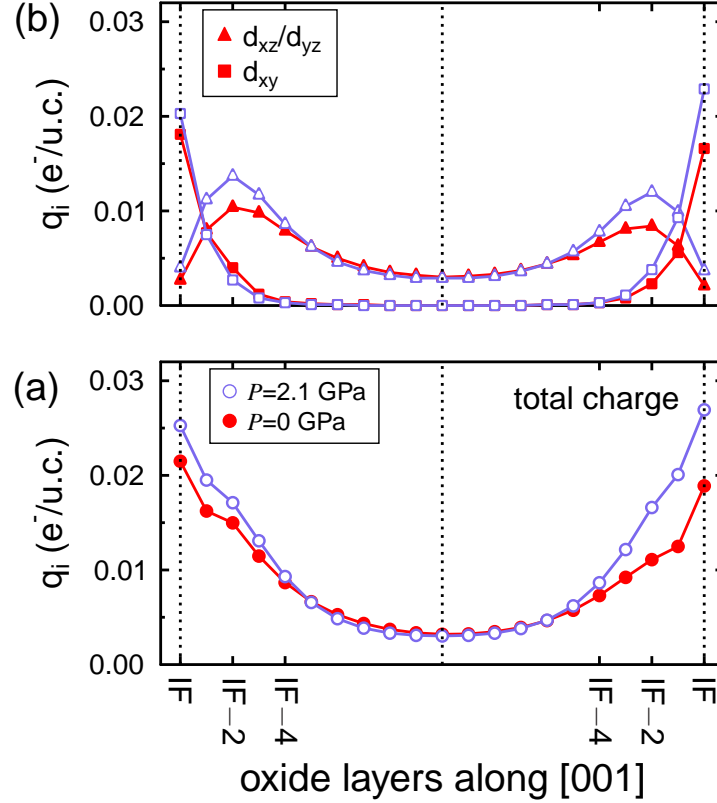


FIG. 22: Charge distribution in the SrTiO_3 part of the fully relaxed $(\text{LaAlO}_3)_5/(\text{SrTiO}_3)_{20.5}/(\text{LaAlO}_3)_5$ slab at zero pressure and $P = 2.1$ GPa. Total electronic charge (a) and its d_{xy} and d_{xz}/d_{yz} components (b) are presented.

- ¹ A. Ohtomo and H. Y. Hwang, A high-mobility electron gas at the $\text{LaAlO}_3/\text{SrTiO}_3$ heterointerface, *Nature* **427**, 423 (2004).
- ² W. Paul and T. Suski, editors, High pressure semiconductor physics I & II, volume 54-55, Elsevier Science (1998).
- ³ J. S. Schilling, Handbook of High-Temperature Superconductivity: Theory and Experiment, chapter High-Pressure Effects, Springer New York (2007).
- ⁴ A. P. Drozdov, M. I. Eremets, I. A. Troyan, V. Ksenofontov, and S. I. Shylin, Conventional superconductivity at 203 kelvin at high pressures in the sulfur hydride system, *Nature* **525**, 73 (2015).
- ⁵ J. H. Haeni, P. Irvin, W. Chang, R. Uecker, P. Reiche, Y. L. Li, S. Choudhury, W. Tian, M. E. Hawley, B. Craigo, A. K. Tagantsev, X. Q. Pan, S. K. Streiffer, L. Q. Chen, S. W. Kirchoefer, J. Levy, and D. G. Schlom, Room-temperature ferroelectricity in strained SrTiO_3 , *Nature* **430**, 758 (2004).
- ⁶ C. W. Bark, D. A. Felker, Y. Wang, Y. Zhang, H. W. Jang, C. M. Folkman, J. W. Park, S. H. Baek, H. Zhou, D. D. Fong, X. Q. Pan, E. Y. Tsymbal, M. S. Rzchowski, and C. B. Eom, Tailoring a two-dimensional electron gas at the $\text{LaAlO}_3/\text{SrTiO}_3$ (001) interface by epitaxial strain, *Proc. Natl. Acad. Sci. U. S. A.* **108**, 4720 (2011).
- ⁷ S. Nazir, M. Behtash, and K. Yang, Enhancing interfacial conductivity and spatial charge confinement of $\text{LaAlO}_3/\text{SrTiO}_3$ heterostructures via strain engineering, *Appl. Phys. Lett.* **105** (2014).
- ⁸ S. Nazir and K. Yang, First-Principles Characterization of the Critical Thickness for Forming Metallic States in Strained $\text{LaAlO}_3/\text{SrTiO}_3$ (001) Heterostructure, *ACS Appl. Mater. Inter.* **6**, 22351 (2014).
- ⁹ C. W. Hicks, M. E. Barber, S. D. Eddins, D. O. Brodsky, and A. P. Mackenzie, Piezoelectric-based apparatus for strain tuning, *Rev. Sci. Instrum.* **85**, 065003 (2014).
- ¹⁰ L. Gao, Y. Y. Xue, F. Chen, Q. Xiong, R. L. Meng, D. Ramirez, C. W. Chu, J. H. Eggert, and H. K. Mao, Superconductivity up to 164 K in $\text{HgBa}_2\text{Ca}_{m-1}\text{Cu}_m\text{O}_{2m+2+\delta}$ ($m=1,2$, and 3) under quasi-hydrostatic pressures, *Phys. Rev. B* **50**, 4260 (1994).
- ¹¹ F. Le Marrec, A. Demuer, D. Jaccard, J. M. Triscone, M. K. Lee, and C. B. Eom, Magnetic behavior of epitaxial SrRuO_3 thin films under pressure up to 23 GPa, *Appl. Phys. Lett.* **80**, 2338 (2002).
- ¹² V. Laukhin, O. Copie, M. J. Rozenberg, R. Weht, K. Bouzehouane, N. Reyren, E. Jacquet, M. Bibes, A. Barthelemy, and G. Herranz, Electronic subband reconfiguration in a d^0 -perovskite induced by strain-driven structural transformations, *Phys. Rev. Lett.* **109**, 226601 (2012).
- ¹³ H. Hilgenkamp, Novel transport phenomena at complex oxide interfaces, *MRS Bull.* **38**, 1026 (2013).
- ¹⁴ S. Thiel, G. Hammerl, A. Schmehl, C. W. Schneider, and J. Mannhart, Tunable quasi-two-dimensional electron gases in oxide heterostructures, *Science* **313**, 1942 (2006).
- ¹⁵ M. Huijben, A. Brinkman, G. Koster, G. Rijnders, H. Hilgenkamp, and D. H. A. Blank, Structure-Property Relation of $\text{SrTiO}_3/\text{LaAlO}_3$ Interfaces, *Adv. Mater.* **21**, 1665 (2009).
- ¹⁶ H. Wadati, D. G. Hawthorn, J. Geck, T. Higuchi, Y. Hikita, H. Y. Hwang, L. F. Kourkoutis, D. A. Muller, S.-W. Huang, D. J. Huang, H.-J. Lin, C. Schuessler-Langeheine, H.-H. Wu, E. Schierle, E. Weschke, N. J. C. Ingle, and G. A. Sawatzky, Resonant soft x-ray scattering studies of interface reconstructions in $\text{SrTiO}_3/\text{LaAlO}_3$ superlattices, *J. Appl. Phys.* **106**, 083705 (2009).
- ¹⁷ N. Pavlenko, T. Kopp, E. Y. Tsymbal, J. Mannhart, and G. A. Sawatzky, Oxygen vacancies at titanate interfaces: Two-dimensional magnetism and orbital reconstruction, *Phys. Rev. B* **86**, 064431 (2012).
- ¹⁸ Z. S. Popovic, S. Satpathy, and R. M. Martin, Origin of the Two-Dimensional Electron Gas Carrier Density at the LaAlO_3 on SrTiO_3 Interface, *Phys. Rev. Lett.* **101**, 256801 (2008).
- ¹⁹ M. Salluzzo, J. C. Cezar, N. B. Brookes, V. Bisogni, G. M. De Luca, C. Richter, S. Thiel, J. Mannhart, M. Huijben, A. Brinkman, G. Rijnders, and G. Ghiringhelli, Orbital Reconstruction and the Two-Dimensional Electron Gas at the $\text{LaAlO}_3/\text{SrTiO}_3$ Interface, *Phys. Rev. Lett.* **102**, 166804 (2009).
- ²⁰ D. Fuchs, A. Sleem, R. Schäfer, A. G. Zaitsev, M. Meffert, D. Gerthsen, R. Schneider, and H. v. Löhneysen, Incipient localization of charge carriers in the two-dimensional electron system in $\text{LaAlO}_3/\text{SrTiO}_3$ under hydrostatic pressure, *Phys. Rev. B* **92**, 155313 (2015).
- ²¹ S. Ernst, A. R. Goñi, K. Syassen, and K. Eberl, Collapse of the Hartree term of the Coulomb interaction in a very dilute 2D electron gas, *Phys. Rev. Lett.* **72**, 4029 (1994).
- ²² C. W. Schneider, S. Thiel, G. Hammerl, C. Richter, and J. Mannhart, Microlithography of electron gases formed at interfaces in oxide heterostructures, *Appl. Phys. Lett.* **89** (2006).
- ²³ M. Altmeyer, H. O. Jeschke, O. Hijano-Cubelos, C. Martins, F. Lechermann, K. Koepnik, A. Santander-Syro, M. J. Rozenberg, R. Valenti, and M. Gabay, Magnetism, spin texture and in-gap states: Atomic specialization at the surface of oxygen-deficient SrTiO_3 , arXiv preprint arXiv:1511.08614, *Phys. Rev. Lett.* (in press) (2015).
- ²⁴ V. Borisov, S. Ostanin, and I. Mertig, Two-dimensional electron gas and its electric control at the interface between ferroelectric and antiferromagnetic insulator studied from first principles, *Phys. Chem. Chem. Phys.* **17**, 12812 (2015).
- ²⁵ P. E. Blöchl, Projector augmented-wave method, *Phys. Rev. B* **50**, 17953 (1994).
- ²⁶ G. Kresse and J. Furthmüller, Efficient iterative schemes for *ab initio* total-energy calculations using a plane-wave basis set, *Phys. Rev. B* **54**, 11169 (1996).
- ²⁷ J. Hafner, Ab-initio simulations of materials using VASP: Density-functional theory and beyond, *J. Comp. Chem.* **29**, 2044 (2008).
- ²⁸ J. P. Perdew, K. Burke, and M. Ernzerhof, Generalized gradient approximation made simple, *Phys. Rev. Lett.* **77**, 3865 (1996).
- ²⁹ S. L. Dudarev, G. A. Botton, S. Y. Savrasov, C. J. Humphreys, and A. P. Sutton, Electron-energy-loss spectra and the

- structural stability of nickel oxide: An LSDA+ U study, Phys. Rev. B **57**, 1505 (1998).
- ³⁰ M. T. Czyzyk and G. A. Sawatzky, Local-density functional and on-site correlations: The electronic structure of La_2CuO_4 and LaCuO_3 , Phys. Rev. B **49**, 14211 (1994).
 - ³¹ P. E. Blöchl, O. Jepsen, and O. K. Andersen, Improved tetrahedron method for Brillouin-zone integrations, Phys. Rev. B **49**, 223 (1994).
 - ³² K. Momma and F. Izumi, VESTA 3 for three-dimensional visualization of crystal, volumetric and morphology data, J. Appl. Cryst. **44**, 1272 (2011).
 - ³³ H. Chen, A. M. Kolpak, and S. Ismail-Beigi, Electronic and Magnetic Properties of c Interfaces from First Principles, Adv. Mater. **22**, 2881 (2010).
 - ³⁴ R. Pentcheva and W. E. Pickett, Avoiding the Polarization Catastrophe in LaAlO_3 Overlayers on SrTiO_3 (001) through Polar Distortion, Phys. Rev. Lett. **102**, 107602 (2009).
 - ³⁵ N. Pavlenko and T. Kopp, Structural relaxation and metal-insulator transition at the interface between SrTiO_3 and LaAlO_3 , Surf. Sci. **605** (2011).
 - ³⁶ S. Piskunov, E. Heifets, R. Eglitis, and G. Borstel, Bulk properties and electronic structure of SrTiO_3 , BaTiO_3 , PbTiO_3 perovskites: an *ab initio* HF/DFT study, Comput. Mater. Sci. **29**, 165 (2004).
 - ³⁷ A. Joshua, S. Pecker, J. Ruhman, E. Altman, and S. Ilani, A universal critical density underlying the physics of electrons at the $\text{LaAlO}_3/\text{SrTiO}_3$ interface, Nat. Commun. **3** (2012).
 - ³⁸ Y. Xie, C. Bell, Y. Hikita, S. Harashima, and H. Y. Hwang, Enhancing Electron Mobility at the $\text{LaAlO}_3/\text{SrTiO}_3$ Interface by Surface Control, Adv. Mater. **25**, 4735 (2013).
 - ³⁹ A. H. Romero and F. Muñoz, *PyProcar* code (available at <https://sourceforge.net/projects/pyprocar/>). (2013).
 - ⁴⁰ R. D. King-Smith and D. Vanderbilt, Theory of polarization of crystalline solids, Phys. Rev. B **47**, 1651 (1993).
 - ⁴¹ N. A. Spaldin, A beginner's guide to the modern theory of polarization, J. Solid State Chem. **195**, 2 (2012).
 - ⁴² G. Berner, A. Müller, F. Pfaff, J. Walde, C. Richter, J. Mannhart, S. Thiess, A. Gloskovskii, W. Drube, M. Sing, and R. Claessen, Band alignment in $\text{LaAlO}_3/\text{SrTiO}_3$ oxide heterostructures inferred from hard x-ray photoelectron spectroscopy, Phys. Rev. B **88**, 115111 (2013).
 - ⁴³ Y. Segal, J. H. Ngai, J. W. Reiner, F. J. Walker, and C. H. Ahn, X-ray photoemission studies of the metal-insulator transition in $\text{LaAlO}_3/\text{SrTiO}_3$ structures grown by molecular beam epitaxy, Phys. Rev. B **80**, 241107 (2009).
 - ⁴⁴ P. Delugas, V. Fiorentini, and A. Filippetti, Dielectric properties and long-wavelength optical modes of the high- κ oxide LaAlO_3 , Phys. Rev. B **71**, 134302 (2005).
 - ⁴⁵ M. Gajdoš, K. Hummer, G. Kresse, J. Furthmüller, and F. Bechstedt, Linear optical properties in the projector-augmented wave methodology, Phys. Rev. B **73**, 045112 (2006).
 - ⁴⁶ G. A. Samara, Pressure and Temperature Dependences of the Dielectric Properties of the Perovskites BaTiO_3 and SrTiO_3 , Phys. Rev. **151**, 378 (1966).
 - ⁴⁷ E. Hegenbarth and C. Frenzel, Pressure dependence of dielectric constants of SrTiO_3 and $\text{Ba}_{0.05}\text{Sr}_{0.95}\text{TiO}_3$ At Low Temperatures, Cryogenics **7**, 331 (1967).
 - ⁴⁸ G. Martin and E. Hegenbarth, Investigation of pressure effects on solid $(\text{Ba}_x\text{Sr}_{1-x}\text{TiO}_3)$ solutions ($x < 0.1$) and SrTiO_3 at low temperatures, Journal of Low Temperature Physics **18**, 101 (1975).
 - ⁴⁹ R. P. Wang, N. Sakamoto, and M. Itoh, Effects of pressure on the dielectric properties of $\text{SrTi}^{18}\text{O}_3$ and $\text{SrTi}^{16}\text{O}_3$ single crystals, Physical Review B **62**, R3577 (2000).
 - ⁵⁰ L. Yu and A. Zunger, A polarity-induced defect mechanism for conductivity and magnetism at polar/nonpolar oxide interfaces, Nat. Commun. **5**, 1 (2014).
 - ⁵¹ J. Zhou, T. C. Asmara, M. Yang, G. A. Sawatzky, Y. P. Feng, and A. Rusydi, Interplay of electronic reconstructions, surface oxygen vacancies, and lattice distortions in insulator-metal transition of $\text{LaAlO}_3/\text{SrTiO}_3$, Phys. Rev. B **92**, 125423 (2015).
 - ⁵² G. Berner, M. Sing, H. Fujiwara, A. Yasui, Y. Saitoh, A. Yamasaki, Y. Nishitani, A. Sekiyama, N. Pavlenko, T. Kopp, C. Richter, J. Mannhart, S. Suga, and R. Claessen, Direct k -Space Mapping of the Electronic Structure in an Oxide-Oxide Interface, Phys. Rev. Lett. **110**, 247601 (2013).
 - ⁵³ One should note here that the resulting lattice constant depends on the choice of U_{eff} parameters in the GGA+ U approach. Pure GGA calculation ($U_{\text{eff}} = 0$) gives the equilibrium a_{\perp} value of 3.864 Å.
 - ⁵⁴ A more detailed analysis of the multiband character evolution with P will be shown elsewhere (P. Seiler, J. Zabaleta *et al.* in preparation).
 - ⁵⁵ Note that this pressure zero may be shifted with respect to the experiment.
 - ⁵⁶ Fixing the two surfaces is needed, since otherwise the full relaxation of all internal positions would have released the pressure in the growth direction due to the existence of the vacuum side.
 - ⁵⁷ Additional relaxation with fixed positions of the LaAlO_3 surfaces changes the stress tensor, which becomes slightly anisotropic. However, the degree of anisotropy is so small that one can still speak of isotropic hydrostatic-like pressure conditions.
 - ⁵⁸ Experimental results of our work and Ref. 20 demonstrate, however, that the observed pressure effects are reversible.